Bifunctional $Cu_{2-x}Se$-decorated hierarchical TiO_2 nanotube mesh with solar water evaporation and photodegradation effects for clean water generation

Peng Ren and Xiuchun Yang

ABSTRACT

The desalination and purification of sea or brackish water by utilizing solar energy are considered to be the most feasible solutions to overcome the problems of water shortage and pollution. In this study, a bifunctional $Cu_{2-x}Se$-decorated hierarchical TiO_2 nanotube mesh (CTNM) was designed and synthesized successfully for both solar water evaporation and photodegradation. $Cu_{2-x}Se$ enhances solar light absorption and solar water evaporation performance as a low-cost absorber because of its localized surface plasmon resonance (LSPR) effect. Meanwhile, the formation of the p-$Cu_{2-x}Se$/n-TiO_2 heterojunction improves the photodegradation performance by increasing separation and transport of photogenerated charge carriers. Hence, CTNM has a relatively high solar water evaporation conversion efficiency of 83.06% and also can photodegrade 95% of methyl orange after 3 h under 2.5 kW m^{-2} simulated solar irradiation, which demonstrate the extremely high utilization ratio of solar energy of CTNM.

Key words | bifunction, clean water generation, $Cu_{2-x}Se$, hierarchical TiO_2 nanotube mesh, photodegradation, solar water evaporation

Peng Ren
Xiuchun Yang (corresponding author)
School of Materials Science and Engineering,
Tongji University,
Shanghai 201804,
China
E-mail: *yangxc@tongji.edu.cn*

Xiuchun Yang
Key Laboratory of Advanced Civil Engineering Materials, Ministry of Education,
Tongji University,
Shanghai 201804,
China

INTRODUCTION

Water is the foundation of human origin and continuation. Rapid industrial growth and the worldwide population explosion have brought about an extremely increased demand for fresh water. Moreover, the contamination of rivers and lakes by industrial wastes and the large amounts of sewage discharged aggravate the serious global problem of water scarcity (Kalogirou 2005).

Many efforts have been made to search for effective solutions to the problem of water shortage, and the desalination of sea or brackish water is the most feasible solution to overcome the problem because the only nearly inexhaustible water sources are the oceans. The traditional water desalination technologies create a series of problems such as energy consumption and environmental pollution caused by utilizing fossil fuels (Elminshawy *et al.* 2015). Therefore, nanomaterials that utilize solar energy to evaporate water become significant for clean water generation (Zhou *et al.* 2016; Ye *et al.* 2017; Guo *et al.* 2018; Ren & Yang 2018).

As is well known, some contaminants in seawater such as alcohol, aldehyde, ketone, phenol and dyestuff that can also form azeotropic mixtures with water can be evaporated during water evaporation (Janakey *et al.* 2018), which can be finally converted to CO_2 and H_2O by photodegradation. So, if the photothermal material possesses both solar water evaporation and photodegradation performance, the processes of water desalination and purification can obviously be simplified. Bifunctional membranes possessing both TiO_2 nanoparticle-based photocatalytic function and Au nanoparticle-based solar water evaporation have been reported (Liu *et al.* 2016; Huang *et al.* 2017), but the noble

doi: 10.2166/ws.2019.076

metal nanostructures are unstable under long periods of irradiation and heating with high cost. In this paper, $Cu_{2-x}Se$ is chosen to decorate TiO_2 nanotube mesh (TNTM) for photothermal conversion and photocatalytic degradation because of excellent solar absorptivity, good photostability, low cytotoxicity and low production cost (Dorfs *et al.* 2011; Hessel *et al.* 2011). The p–n heterojunction between p-$Cu_{2-x}Se$ ($E_g = 1.35$ eV) and n-TiO_2 nanotube (NT) favors the fast separation and transport of photogenerated charge carriers along the tube wall, which improves the photodegradation performance of the hybrid material (Ratanatawanate *et al.* 2009; Zhou *et al.* 2011; Han *et al.* 2015). In addition, TNTM with many radial NTs around Ti wires also positively influences the performance because of its large specific surface area, flexibility and light absorption independent of the direction of the solar light (Yang & Chen 2016). Hence, the CTNM exhibits a relatively high solar water evaporation conversion efficiency of 83.06% and an excellent methyl orange (MO) photodegradation efficiency of 95% in 3 h under 2.5 kW m^{-2} simulated solar irradiation.

METHODS

Preparation of TNTM

A large piece of raw Ti mesh was cut into square pieces of 2.5×2.5 cm^2, which were ultrasonically degreased in acetone, isopropanol and methanol for 15 min respectively, and then chemically etched in a mixture of HF and HNO_3 aqueous solution ($HF:HNO_3:H_2O = 1:4:10$ by volume) for 10 s, afterwards rinsed with deionized water and finally dried in air. Electrochemical anodic oxidation was performed at 60 V direct current voltage for 24 h in diethylene glycol solution containing 1.5 vol% HF, using Ti mesh as the working electrode and Pt plate as counter-electrode. The as-prepared samples were ultrasonically rinsed with deionized water and dried in air. To convert samples from amorphous phase to anatase phase, thermal treatment was performed in air at 450 °C for 3 h.

Preparation of CTNM

All experiments were performed with a LK98BΠ electrochemical workstation using the TNTM as the working electrode, platinum plate as counter electrode and saturated calomel electrode as reference electrode, respectively. Cu_3Se_2 was electrochemically deposited into TiO_2 NT channels in 30 mL fresh electrolyte containing 0.1 M $CuSO_4{\cdot}5H_2O$ and 0.05 M H_2SeO_3 aqueous solution. Pulse electro-deposition was adopted with a pulse voltage of −0.45 V, a pulse time of 1 s and an interval time of 4 s, which permitted depleted ion equilibrium in the interval time. Cu_3Se_2-decorated TNTM with 10, 30 and 50 electrochemical cycles was taken out from the electrolyte and rinsed with deionized water, then dried in air, respectively. To convert Cu_3Se_2 into $Cu_{2-x}Se$, thermal treatment was performed in N_2 at 300 °C for 3 h.

Solar water evaporation

The solar water evaporation performances of all samples were tested in a nested cubic container with a test room of a surface area of 2.7×2.7 cm^2 and a depth of 3 cm. The container was placed on an electronic balance to measure the weight of evaporated water. For each run, the container was filled with deionized water, and the sample on supporting glass-fiber cotton floated on the water surface. A 500 W xenon lamp was used to simulate solar irradiation and the aperture diameter was adjusted to be the same on the sample each time. After certain time intervals, the weight of water in the container was recorded. A K-type thermocouple was used to measure the temperature of the surface water and the temperatures were recorded after certain time intervals (Figure S1, Supplementary Material, available with the online version of this paper).

Photodegradation activity test

Photodegradation activity of the samples was evaluated by decomposing 10^{-5} M MO solution under the 500 W Xe lamp. Before photodegradation, MO adsorption equilibrium on the sample surface was established by mechanical stirring in the dark for 30 min. The MO concentration was recorded at every simulated solar light irradiation time interval of 60 min at 462 nm by UV1700 UV-Vis spectrophotometer.

RESULTS AND DISCUSSION

The X-ray diffraction (XRD) patterns in Figure 1(a) indicate that tetragonal Cu_3Se_2 (JCPDS card No. 47-1745) is successfully deposited by the electrochemical deposition method into TNTM prepared through the electrochemical anodic oxidation method (Gong *et al.* 2001) and converted into $Cu_{2-x}Se$ after thermal treatment because six new peaks appear at 26.75°, 44.60°, 52.91°, 64.98°, 71.59° and 82.24°, which can be assigned to the (111), (220), (311), (400), (331) and (422) crystal faces of $Cu_{2-x}Se$ (JCPDS card No. 06-0680). The samples with 10, 30 and 50 pulse cycles were denoted as O-10, O-30 and O-50, and S-10, S-30 and S-50 after thermal treatment, respectively.

The electrochemical reaction is described by Equation (1):

$$3Cu^{2+} + 2H_2SeO_3 + 8H^+ + 14e^- \rightarrow Cu_3Se_2 + 6H_2O \quad (1)$$

The phase transformation during thermal treatment can be depicted as:

$$\underset{Tetragonal-a=b=6.403\,\text{Å},c=4.278\,\text{Å}}{Cu_3Se_2} \rightarrow \underset{Cubic-a=b=c=5.739\,\text{Å}}{Cu_{2-x}Se} \quad (2)$$

The $Cu_{2-x}Se$ phase content increases with pulse cycles based on the intensity of the $Cu_{2-x}Se$ peaks. According to the Scherrer equation, the calculated $Cu_{2-x}Se$ grain size is

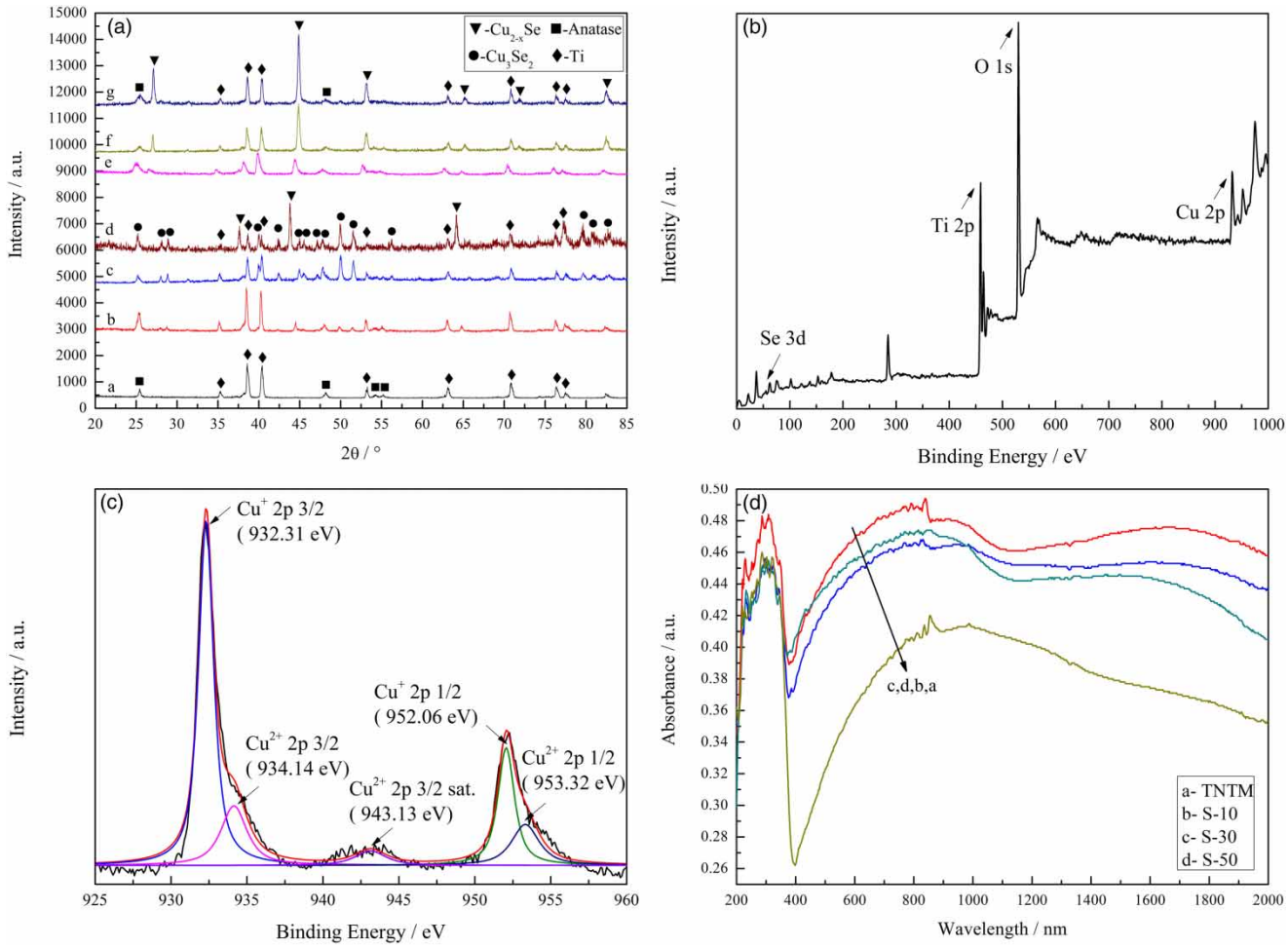

Figure 1 | (a) XRD patterns of samples TNTM (curve a), O-10 (curve b), O-30 (curve c), O-50 (curve d), S-10 (curve e), S-30 (curve f) and S-50 (curve g); (b) XPS survey spectrum of S-30; (c) experimental and fitted Cu 2p XPS spectrum of S-30; (d) UV-Vis-NIR absorption spectra of samples TNTM, S-10, S-30 and S-50.

14 nm, 21 nm, and 39 nm for samples S-10, S-30 and S-50, respectively. Figure 1(b) and 1(c) show the X-ray photoelectron spectroscopy (XPS) spectra of the sample S-30. From the XPS survey spectrum in Figure 1(b) it turns out that the sample contains Cu, Ti, O and Se elements. The high resolution XPS spectrum of Cu in Figure 1(c) indicates the existence of Cu^{2+} ions in sample S-30 because of the partial oxidization of Cu^{+} ions at the surface.

The ultraviolet-visible-near infrared (UV-Vis-NIR) absorption spectra of TNTM, S-10, S-30 and S-50 (Figure 1(d)) indicate that TNTM mainly absorbs ultraviolet light with an absorption edge at about 387 nm corresponding to the band gap of anatase TiO_2 (about 3.2 eV). The wide absorption around 1,000 nm can be attributed to oxygen vacancies and Ti^{3+} ions (Kagan *et al.* 1999). The decoration of $Cu_{2-x}Se$ extends the absorption range of TiO_2 from 400 nm to 2,000 nm. Compared with S-10 with insufficient $Cu_{2-x}Se$ and S-50 with too much $Cu_{2-x}Se$, S-30 has the highest absorbance due to the appropriate $Cu_{2-x}Se$ quantity that not only enhances light absorption but also does not obstruct the light absorption of the NT structure, which can effectively trap light in extremely long and narrow inter-NT channels such that the light can hardly escape. In addition, the localized surface plasmon resonance (LSPR) peaks at about 1,700 nm can be observed in spectra of S-10, S-30 and S-50, which have a slight red shift and widen with the decrease of grain size and nanoparticle size (Smithard 1973; Ganière *et al.* 1975).

Figure 2 shows scanning electron microscope (SEM) images and energy dispersive spectroscopy (EDS) spectra of TNTM, S-10, S-30 and S-50. Figure 2(a) indicates that vertically oriented TiO_2 NTs separate from each other with a tube diameter of about 165 nm and a wall thickness of about 43 nm. The sideview image in Figure 2(b) indicates that the tube length is about 3.5 μm. Figure 2(d) and 2(f) indicate that a few $Cu_{2-x}Se$ are deposited on the tube openings and walls for ten cycles. After 30 cycles, the NT surface becomes extensively coated with relatively uniform $Cu_{2-x}Se$ (Figure 2(g) and 2(h)). With further increase of deposition to 50 cycles, obvious agglomerations of $Cu_{2-x}Se$ are observed on the top surface of the TiO_2 NTs which partially block the NT channels (Figure 2(j) and 2(k)).

Figure 3 depicts the surface water temperature and evaporated water mass changes when 2.5 kW m^{-2} simulated solar light irradiates the samples floating on the surface of the deionized water over time. $Cu_{2-x}Se$ was deposited on Ti mesh for 30 cycles as a control sample denoted as TCS.

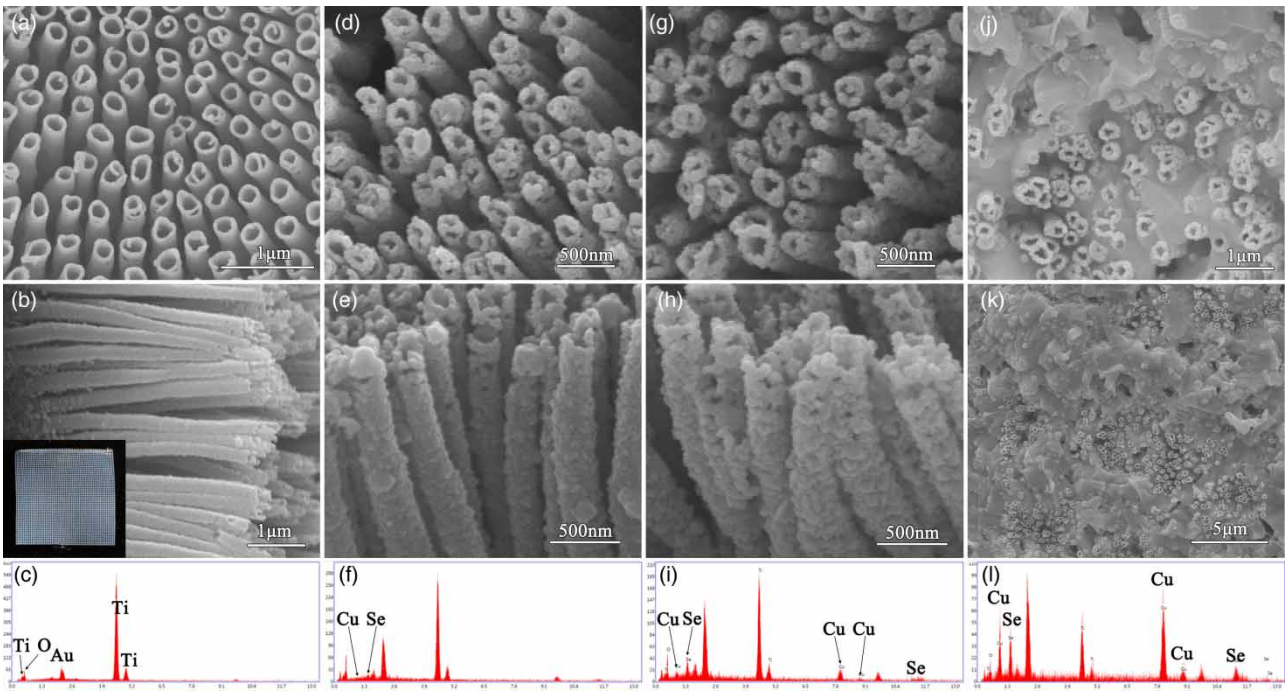

Figure 2 | SEM images and EDS spectra of TNTM (a)–(c), S-10 (d)–(f), S-30 (g)–(i) and S-50 (j)–(l); the inset shows the optical image of TNTM.

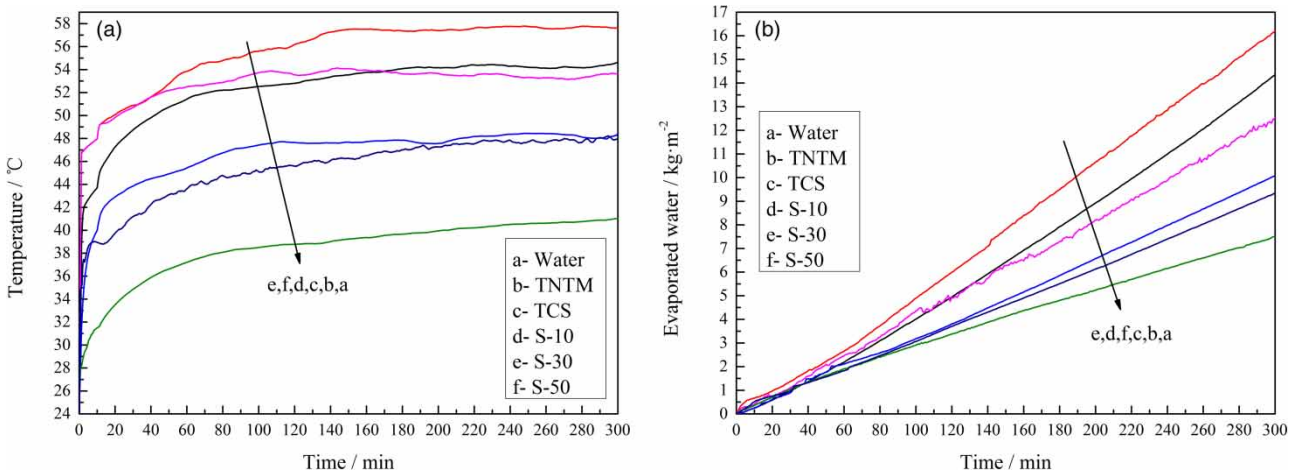

Figure 3 | (a) Surface water temperature and (b) evaporated water mass changes under 2.5 kW m^{-2} simulated solar irradiation over time with water itself, and samples TNTM, TCS, S-10, S-30, and S-50.

The surface water temperature and the evaporated water mass increase with the irradiation time. Especially, S-30 has the highest final surface water temperature (57.7 °C), which is obtained by fitting the temperature values in the last 1 h and the largest evaporated water mass (16.141 kg m^{-2}). Compared with S-30, S-10 and S-50 have lower surface water temperature and evaporated water mass values due to the low utilization efficiency for solar light. The sample TNTM and the sample TCS have similar surface water temperature and evaporated water mass values.

The solar water evaporation conversion efficiency (η) is an important index to evaluate a solar photothermal conversion material for water evaporation. Table S1 (Supplementary Material, available with the online version of this paper) summarizes the calculated η values indicating that S-30 possesses the highest η of 83.06%, and S-10 and S-50 have a little lower η values of 73.15% and 62.54%, respectively. TNTM has the lowest η of 46.14%. In addition, TCS has an η value of 50.37%, a little higher than TNTM.

Figure 4(a) shows the degradation efficiencies of samples TNTM, TCS, S-10, S-30 and S-50 under 2.5 kW m^{-2} simulated solar light irradiation. For comparison purposes, the autodecomposition of the MO aqueous solution under the same simulated solar light irradiation was studied, and its final photodegradation rate was 3%. After 3 h of simulated solar irradiation, 95% of MO was decomposed by S-30, and only 85%, 60%, 74% and 6% of MO was decomposed by S-10, S-50, TNTM and TCS, respectively. As shown in Figure 4(b), S-30 exhibits the highest photodegradation rate constant (k), which is about 3.3 times as high as that of TNTM. Furthermore, its k value increases over time because the concentrating of heat by photothermal conversion gradually improves the rate of photodegradation reactions. S-10 and S-50 had higher k than TNTM, by about 2.1 times and 1.5 times, respectively.

According to the experimental and theoretical analysis, the energy band structure diagram of the p-$Cu_{2-x}Se$/n-TiO_2 heterojunction is expounded schematically in Figure 4(c). It is well known that the photocatalytic activities of photocatalysts mainly depend on the separation and transport of photogenerated charge carriers. When the p-$Cu_{2-x}Se$ and n-TiO_2 are combined to form the p–n heterojunction, an interfacial electric field is built in the interface between $Cu_{2-x}Se$ and TiO_2, which leads to the upward band bending of n-TiO_2 and downward band bending of p-$Cu_{2-x}Se$ (Zhang & Yates 2012; Han *et al.* 2015).

Under simulated solar light irradiation, $Cu_{2-x}Se$ acting as a photosensitizer can be easily activated by solar light and generated electrons and holes. The photogenerated electron–hole pairs are separated effectively in the p-$Cu_{2-x}Se$/n-TiO_2 heterojunction interface. The efficient charge separation can increase the lifetime of the charge carriers and give them enough time to react with the reactants adsorbed onto the photocatalyst surfaces so as to improve the photodegradation activity. In such a case, the photogenerated electrons can reduce the oxygen to generate

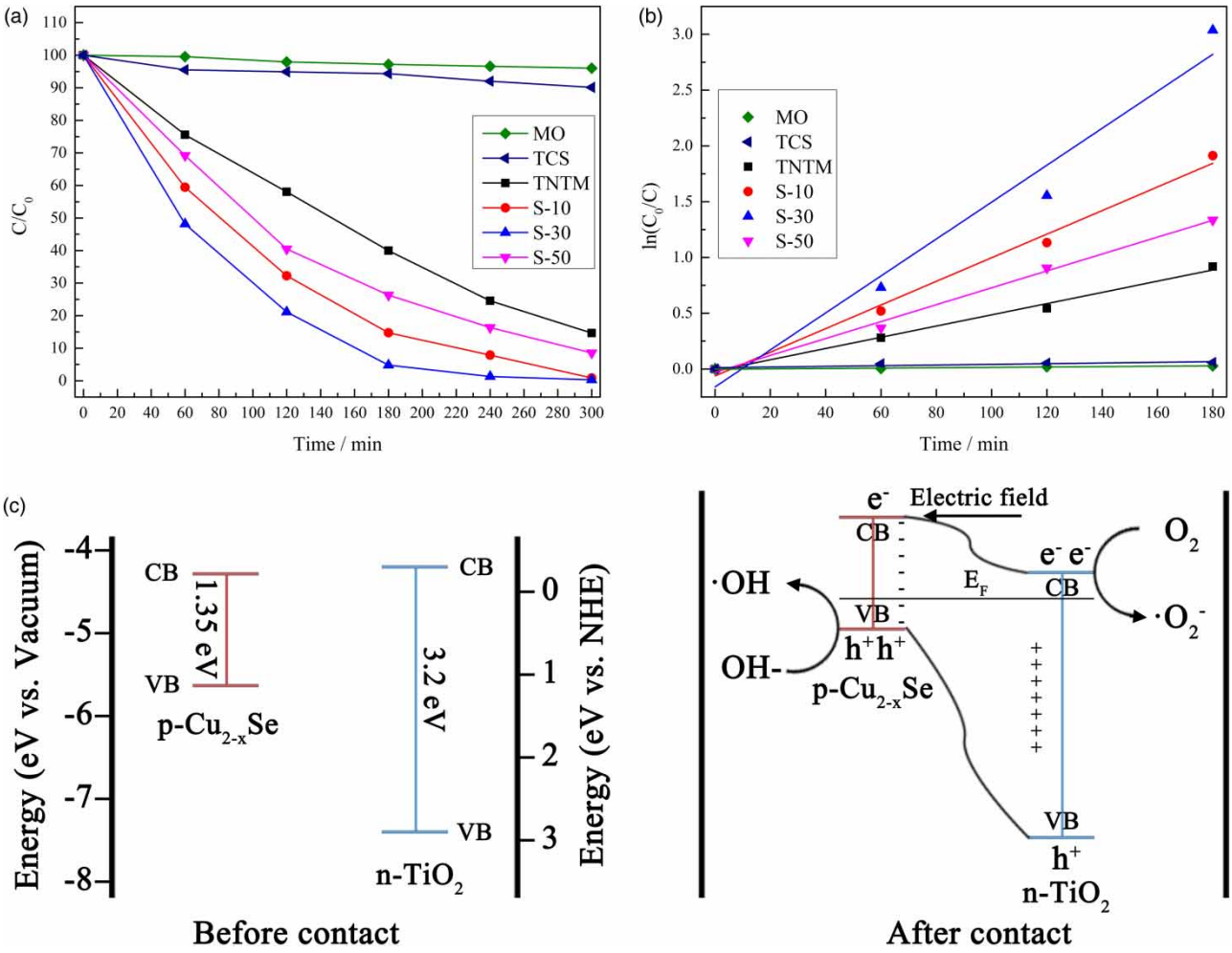

Figure 4 | (a) Photodegradation of MO and (b) a plot of $\ln(C_0/C)$ versus irradiation time with MO solution itself, and samples TCS, TNTM, S-10, S-30, and S-50; (c) the energy band structure diagrams of $Cu_{2-x}Se$ and TiO_2 before and after contact. (CB: conduction band, VB: valence band, NHE: normal hydrogen electrode.)

the active species $\cdot O_2^-$, which can further lead to oxidation of MO. The holes would be readily scavenged by H_2O or OH^-, leading to ·OH radicals, and accelerating the MO degradation.

Figure S2 (Supplementary Material, available online) shows the schematic diagram of solar water evaporation and photodegradation processes for sample CTNM. When the simulated solar light irradiates samples, light is effectively trapped in inter-NT channels. Moreover, the radial NTs around Ti wires can absorb light from different directions so that the utilization efficiency of solar light is further improved. Meanwhile, CTNM absorbs photon energy by the two mechanisms of LSPR (Herzog *et al.* 2014) and electron transitions (intraband transition and interband transition) (Yang *et al.* 2009) that make CTNM sufficiently utilize the light in the solar spectrum. The photogenerated hot electrons on the CB of the TiO_2 and $Cu_{2-x}Se$ participate in the photodegradation reaction. The other hot electrons relax initially by electron–electron scattering, which transfer their energy to lattices and cool via inelastic electron–phonon collisions. Finally, phonon–phonon interactions result in a complete relaxation of the initially absorbed photon energy to make TiO_2 NTs and $Cu_{2-x}Se$ become hot. Therefore, CTNM can almost completely convert the absorbed light into thermal and chemical energy. The photodegradation process is closely associated with evaporation. Photodegradation takes

place in the $Cu_{2-x}Se$-decorated TiO_2 NT channels when accompanied by water evaporation. The concentration of $Cu_{2-x}Se$ can also be increased in TiO_2 NT channels rather than the $Cu_{2-x}Se$ dispersing into the bulk solution to improve the efficiency of photodegradation (Huang *et al.* 2017). Thus, the TiO_2 NT channels play a key role in concentrating $Cu_{2-x}Se$ for photodegradation, while also concentrating heat for water evaporation that can increase the rate of the photodegradation reaction (Clavero 2014). Water evaporation also makes MO solution be transported to the NT channels and degraded. Additionally, the NT channels are able to absorb the MO through the water evaporation process. The more water is evaporated, the more MO the NT channels can absorb, leading to a decrease in the concentration of MO.

Previously, the loss of energy efficiency in photocatalytic water purification has been the result of two processes: the absorption process with the relatively narrow absorption bands of the photocatalysts and photothermal conversion with the absorbed photons (Liu *et al.* 2016). The integration of the photothermal-driven solar water evaporation function with the photodegradation function helps expand the range of useful solar light for clean water generation and also takes advantage of the heat generated by the catalysts for further efficiency enhancement. The bifunctional CTNM enables the generation of both pure and partially purified water in a single step. Pure water is generated through the solar water evaporation process and partially purified water is the result of the photodegradation process.

CONCLUSION

In summary, CTNM was successfully synthesized by annealing Cu_3Se_2-decorated hierarchical TiO_2 NT mesh, which was fabricated by electrochemical methods. The LSPR peak has a slight red shift and widens with the decrease of grain size and nanoparticle size resulting from the decrease of electrochemical deposition cycles. Moderate amounts of $Cu_{2-x}Se$ dramatically improve the light absorption, solar water evaporation and photodegradation performances. S-30 has a relatively high solar water evaporation conversion efficiency of 83.06% and also can photodegrade 95% of MO after 3 h under 2.5 kW m^{-2} simulated solar irradiation. The high solar water evaporation efficiency with the high photodegradation rate demonstrates that CTNM has an extremely high utilization ratio of solar energy. Hence, utilizing CTNM as an efficient and low-cost nanomaterial combining solar water evaporation and photodegradation functions for generating pure and purified water is a promising approach to address the dual issues of fresh water shortage and water pollution.

REFERENCES

Clavero, C. 2014 Plasmon-induced hot-electron generation at nanoparticle/metal-oxide interfaces for photovoltaic and photocatalytic devices. *Nat. Photonics* **8** (2), 95–103.

Dorfs, D., Härtling, T., Miszta, K., Bigall, N. C., Kim, M. R., Genovese, A., Falqui, A., Povia, M. & Manna, L. 2011 Reversible tunability of the near-infrared valence band plasmon resonance in $Cu_{2-x}Se$ nanocrystals. *J. Am. Chem. Soc.* **133** (29), 11175–11180.

Elminshawy, N. A. S., Siddiqui, F. R. & Sultan, G. I. 2015 Development of a desalination system driven by solar energy and low grade waste heat. *Energ. Convers. Manage.* **103**, 28–35.

Ganière, J.-D., Rechsteiner, R. & Smithard, M.-A. 1975 On the size dependence of the optical absorption due to small metal particles. *Solid State Commun.* **16** (1), 113–115.

Gong, D., Grimes, C. A., Varghese, O. K., Hu, W., Singh, R. S., Chen, Z. & Dickey, E. C. 2001 Titanium oxide nanotube arrays prepared by anodic oxidation. *J. Mater. Res.* **16** (12), 3331–3334.

Guo, Z., Ming, X., Wang, G., Hou, B., Liu, X., Mei, T., Li, J., Wang, J. & Wang, X. 2018 Super-hydrophilic copper sulfide films as light absorbers for efficient solar steam generation under one sun illumination. *Semicond. Sci. Technol.* **33** (2), 025008.

Han, J., Zou, H., Liu, Z., Yang, T., Gao, M. & Huang, C. 2015 Efficient visible-light photocatalytic heterojunctions formed by coupling plasmonic $Cu_{2-x}Se$ and graphitic carbon nitride. *New J. Chem.* **39** (8), 6186–6192.

Herzog, J. B., Knight, M. W. & Natelson, D. 2014 Thermoplasmonics: quantifying plasmonic heating in single nanowires. *Nano Lett.* **14** (2), 499–503.

Hessel, C. M., Pattani, V. P., Rasch, M., Panthani, M. G., Koo, B., Tunnell, J. W. & Korgel, B. A. 2011 Copper selenide nanocrystals for photothermal therapy. *Nano Lett.* **11** (6), 2560–2566.

Huang, J., He, Y., Wang, L., Huang, Y. & Jiang, B. 2017 Bifunctional $Au@TiO_2$ core–shell nanoparticle films for clean water generation by photocatalysis and solar evaporation. *Energ. Convers. Manage.* **132**, 452–459.

Janakey Devi, V. K. P., Sai, P. S. T. & Balakrishnan, A. R. 2018 Ammonium-based ionic liquid as an entrainer for the

separation of *n*-propanol + water and isopropanol + water mixtures. *J. Chem. Eng. Data* **63** (3), 498–507.

Kagan, C. R., Mitzi, D. B. & Dimitrakopoulos, C. D. 1999 Organic-inorganic hybrid materials as semiconducting channels in thin-film field-effect transistors. *Science* **286** (5441), 945–947.

Kalogirou, S. A. 2005 Seawater desalination using renewable energy sources. *Prog. Energ. Combust.* **31** (3), 242–281.

Liu, Y., Lou, J., Ni, M., Song, C., Wu, J., Dasgupta, N. P., Tao, P., Shang, W. & Deng, T. 2016 Bioinspired bifunctional membrane for efficient clean water generation. *ACS Appl. Mater. Interfaces* **8** (1), 772–779.

Ratanatawanate, C., Tao, Y. & Balkus, K. J. 2009 Photocatalytic activity of PbS quantum dot/TiO_2 nanotube composites. *J. Phys. Chem. C* **113** (24), 10755–10760.

Ren, P. & Yang, X. 2018 Synthesis and photo-thermal conversion properties of hierarchical titanium nitride nanotube mesh for solar water evaporation. *Sol. RRL* **2** (4), 1700233.

Smithard, M. A. 1973 Size effect on the optical and paramagnetic absorption of silver particles in a glass matrix. *Solid State Commun.* **13** (2), 153–156.

Yang, X. & Chen, C. 2016 Cu_2O sensitized flexible 3D-TiO_2 nanotube arrays for enhancing visible photo-electrochemical performance. *RSC Adv.* **6** (75), 70978–70983.

Yang, X., Dong, Z., Liu, H., Xu, J. & Qian, S. 2009 Effects of thermal treatment on the third-order optical nonlinearity and ultrafast dynamics of Ag nanoparticles embedded in silicate glasses. *Chem. Phys. Lett.* **475** (4–6), 256–259.

Ye, M., Jia, J., Wu, Z., Qian, C., Chen, R., O'Brien, P. G., Sun, W., Dong, Y. & Ozin, G. A. 2017 Synthesis of black TiO_x nanoparticles by Mg reduction of TiO_2 nanocrystals and their application for solar water evaporation. *Adv. Energy Mater.* **7** (4), 1601811.

Zhang, Z. & Yates, J. T. 2012 Band bending in semiconductors: chemical and physical consequences at surfaces and interfaces. *Chem. Rev.* **112** (10), 5520–5551.

Zhou, Q., Fu, M., Yuan, B., Cui, H. & Shi, J. 2011 Assembly, characterization, and photocatalytic activities of TiO_2 nanotubes/CdS quantum dots nanocomposites. *J. Nanopart. Res.* **13** (12), 6661–6672.

Zhou, L., Tan, Y., Ji, D., Zhu, B., Zhang, P., Xu, J., Gan, Q., Yu, Z. & Zhu, J. 2016 Self-assembly of highly efficient, broadband plasmonic absorbers for solar steam generation. *Sci. Adv.* **2** (4), e1501227.

First received 17 February 2019; accepted in revised form 9 May 2019. Available online 21 May 2019